# Boron Nitride Nanotubes Toughen Silica Ceramics

Nasim Anjum,[1] Dingli Wang,[1] Feilin Gou,[1] Changhong Ke[1,2*]

[1]Department of Mechanical Engineering, State University of New York at Binghamton, Binghamton, NY 13902, USA

[2]Materials Science and Engineering Program, State University of New York at Binghamton, Binghamton, NY 13902, USA

*Author to whom correspondence should be addressed: cke@binghamton.edu.

**Abstract**

Boron nitride nanotubes (BNNTs) are promising reinforcing fillers for ceramics because of their extraordinary structural and mechanical properties and thermal stability, but their reinforcing mechanisms remain elusive. Here, we investigate how BNNTs reinforce silica nanocomposites by quantifying their bulk and interfacial mechanical properties using *in situ* Raman micromechanical characterization techniques and microstructural analysis. Our studies reveal that the incorporation of small amounts of BNNTs (0.1 to 0.5 wt.%) substantially increases the flexural strength (~51% to ~153%) and fracture toughness (~44% to ~167%) of silica. The effective interfacial shear stress in the bulk BNNT-silica nanocomposite follows a shear-lag model with a maximum value of ~92 MPa. The microstructural analysis reveals that incorporating BNNTs in silica has a prominent influence on its crystallization, with a noticeable increase in porosity and a decrease in crystal size and lattice strain. The collective microstructural changes substantially contribute to the bulk mechanical properties of the BNNT-silica nanocomposite. The findings provide insights into the reinforcement mechanism of BNNTs in ceramics and contribute to the optimal design of light, strong, tough, and durable ceramic materials.

.

**Keywords**: Boron Nitride Nanotubes; Ceramic Nanocomposites; Fracture Toughness; Interfacial Load Transfer; Microstructures

## 1. Introduction

Ceramics are renowned for their superior mechanical stiffness and strength, chemical inertness, and thermal stabilities, but their intrinsic brittleness substantially limits their engineering applications. Reinforcing the bulk mechanical properties of ceramics with fillers is a possible solution. Boron nitride nanotubes (BNNTs)[1,2] are a promising reinforcing additive for ceramics because of their extraordinary

structural and physical properties.[3,4] BNNTs have a low density of 1.35 g/cm$^3$ and large surface-to-volume ratios. BNNTs are one of the stiffest and strongest known materials with Young's modulus of up to 1.3 TPa and tensile strength of up to 30-60 GPa,[5–14] rivaling those of carbon nanotubes (CNTs). Unlike the weak van der Waals interlayer interaction in CNTs, BNNTs possess strong interlayer binding interactions,[15,16] enabling both exterior and interior tube shells to carry loads within the matrix. The supple characteristics of BNNTs in the transverse direction[17–19] enable them to conform well to ceramic particle surfaces. BNNTs possess extraordinary thermal conductivity (up to 3,000 $Wm^{-1}k^{-1}$)[20] and have superior thermal and chemical stabilities. BNNTs can survive up to 900°C in the air[21] and over 1800°C in an inert gas environment.[22] Our recent studies reveal that the BNNT-ceramic interface possesses rugged anisotropic energy landscapes due to the partially ionic B-N bonding, with nanotube pullout as the dominant interfacial failure mode.[23,24] The high energy barrier resists shear and improves the load transfer across the interface. The strong interfacial binding enables BNNTs to act as crack stoppers in ceramics, while the pullout of nanotubes from the matrix helps dissipate energy via friction. These desirable mechanical and interfacial characteristics underpin the superior reinforcement potentials of BNNTs for ceramics, particularly fracture toughness improvement.

Substantial bulk mechanical property improvements of BNNT-reinforced ceramic nanocomposites have been reported.[25–35] For example, the introduction of 1 wt.% BNNTs in zirconia ($ZrO_2$) and $Al_2O_3$ reportedly increase the ceramic's toughness by 65% and 35%, respectively.[25,26] The addition of 5 wt.% BNNTs in silica ($SiO_2$) reportedly increased the fracture strength by 131% and the fracture toughness by 109%.[27] A recent study reported respective increases in bending modulus and strength by 72% and 55% from the addition of merely 0.1wt.% BNNTs.[28] While these reported bulk mechanical property improvements are useful to demonstrate the reinforcement potentials of BNNTs for ceramics, the underlying reinforcing mechanism remains elusive. This is in part because the interfacial load transfer, which is critical to the mechanical reinforcement, can at most be evaluated indirectly and/or qualitatively from those bulk mechanical measurements and/or microscopic imaging, while quantitative interfacial stress transfer in the bulk BNNT-ceramic nanocomposite remains unexplored. In addition, the incorporation of even tiny amounts of BNNTs may result in substantial microstructural changes of the ceramic matrix (such as crystallinity, grain size, porosity, etc.), thus influencing the overall bulk mechanical properties of the ceramic nanocomposite.[36–38] Therefore, it is of importance to consider both the interfacial load transfer and the microstructural changes to understand the reinforcing mechanism of BNNTs in ceramic nanocomposites.

In this study, we quantitatively investigate the bulk and interfacial mechanical properties of BNNT-reinforced silica using *in situ* Raman micromechanical characterization techniques in conjunction with detailed microstructural analysis. Silica is chosen for its technological relevance to devices and composites and widespread industrial usage. Our studies reveal substantial improvements in the bulk mechanical properties, including flexural strength and fracture toughness, from the addition of small amounts of BNNTs. A shear-lag effect is exhibited in the effective interfacial load transfer inside the bulk BNNT-silica nanocomposite. Our studies reveal the BNNT-induced porosity and crystallinity changes to the underlying ceramic matrix and their contribution to the bulk mechanical enhancement. The findings reported in this work provide critical insights into the reinforcing mechanisms of BNNTs in ceramic nanocomposites and contribute to the optimal design of light, strong, tough, and reliable ceramic-based engineering materials.

## 2. Materials and Methods

### *2.1 Sample Preparations*

The employed BNNTs, which were purchased from BNNT Materials**,** were produced using high-temperature pressure (HTP) methods[39] and contain >99% hexagonal boron nitride (h-BN) per the manufacturer datasheet. Our Fourier transform infrared (FTIR) spectroscopy analysis of the as-received BNNT puffballs using a Nicolet 8700 FTIR spectrometer (see Fig. S1 in the *supporting information*) shows a BNNT purity of ~87-88%. Our recent studies show that a majority (>97%) of HTP-BNNTs are of 1-4 tube walls with a dominance of double-walled structures, and their diameters are poly-dispersed with ~2.9 nm in median diameter.[40,41] The as-received BNNTs were dispersed and separated in ethanol with the aid of ultrasonication[42] using a bath sonicator (155 W, 42 kHz) for 3-6 h. Two types of silica particles with respective diameters of about 1 μm and 20-30 nm (US Research Nanomaterials, Inc.) were mixed in a weight ratio of 9:1. Subsequently, the dispersed BNNT solution was added to the silica powder composition and thoroughly mixed using a cup horn sonicator. The resulting slurry was then dried at 70°C for 12 h.

To fabricate ceramic bars for mechanical measurements, the dried nanocomposite material was first crushed, ground, and then passed through a 150-μm sieve. The obtained fine nanocomposite powders were pressed into rectangular bars using a rectangular steel die (50 mm × 12 mm × 25 mm) under a pressing force of 8,000 lbs at 300°C for 1 h using a Carver 15-ton hot press. The molded ceramic nanocomposite bars were subsequently sintered in nitrogen inside an MTI tube furnace. The sintering was conducted in three stages: (1) The temperature was raised from room temperature to 200°C at a heating rate of 2°C/min

and then held for 20 min; (2) The temperature was further raised to 1200°C at a heating rate of 2.85°C/min and then held for 1 h. (3) The temperature was increased to 1400°C at a heating rate of 1°C/min and held for 1 h. Specimens with five different BNNT weight concentrations (0 wt.%, 0.1 wt.%, 0.2 wt.%, 0.3 wt.%, and 0.5 wt.%) were manufactured using the same procedure. The nanocomposite bars were subsequently polished using a MultiPrep polisher and cut into the respective sizes of two types of rectangular bar specimens (see Fig. S2): (i) single-edge notched bend (SENB) specimen for the fracture toughness measurement with nominal dimensions of length 25 mm, depth 5 mm, thickness 2.5 mm, notch length 2.5 mm and notch root radius 0.5 mm; (ii) unnotched rectangular specimen for the flexural strength measurement with nominal dimensions of length 12 mm, depth 5 mm, thickness 1 mm. The machine tolerance is ~0.1 mm, except for the notch root radius (~0.05 mm).

*2.2 Sample characterization*

Raman micromechanical measurements were conducted, *in situ*, using a Linkam TST350 mechanical tester that is integrated with a Renishaw inVia Raman microscope (532 nm laser and 50× objective lens). The three-point bending measurements were conducted at a loading rate of 2 μm/s and were held for about two minutes for Raman spectrum acquisition at each 10 μm displacement mark of the tester's loading pin. Stand-alone three-point bending measurements of the ceramic nanocomposite bar were conducted using an ADMET universal tensile tester with a loading rate of 2 μm/s. At least five different samples were mechanically characterized for each type of nanocomposite specimen. A Zeiss field emission scanning electron microscope (SEM) was used to image the nanocomposite specimens. Digital image correlation (DIC) measurements were carried out using a DIC system from LaVison that is composed of M-lite 5-Mega pixels cameras with a resolution of 2464 by 2056 pixels, a pixel size of ~3.5 μm, and a recording frame rate of 10 Hz. X-ray diffraction (XRD) measurements were carried out using a Panalytical X-ray Diffractometer. Micro-computed tomography (micro-CT) measurements were conducted using a Phoenix X-ray Imager.

*2.3 Finite Element Simulations*

A 3D finite element model was established to simulate the strain distribution in the SENB-type BNNT-silica nanocomposite specimen under the three-point bending test using commercial code ANSYS. By assuming isotropy and homogeneity of BNNT-silica nanocomposite specimens, three-dimensional volume elements 'SOLID185' with eight nodes and three degrees of freedom per node were used in the simulations.

## 3. Results and discussion

### *3.1 Bulk Mechanical Properties of BNNT-silica nanocomposites*

The fracture toughness of the BNNT-silica nanocomposite was evaluated using the SENB method. Fig. 1a shows the measured rupture force of the notched BNNT-silica specimens, which increases substantially with the BNNT concentration. Notably, the rupture force increases by ~54% from ~9.1 N to ~14.0 N with an addition of 0.1 wt.% BNNTs, while an over 2.6-fold increase with adding 0.5 wt.% BNNTs (see Table 1). The remarkable increase in the rupture force indicates the enhancements of the mechanical strength and the fracture toughness. Fig. 1b shows the measured flexural strength of the unnotched BNNT-silica specimens using three-point bending tests, which exhibits a similar degree of enhancement as the rupture force shown in Fig. 1a. The rupture of the U-notch tip under a three-point loading condition occurs as a mode I fracture. Here, the mean stress criterion is adopted to calculate the fracture toughness $K_{IC}$ of the U-notched beam using the maximum stress $\sigma^m$ at the notch tip and the notch root radius, $R$. The mean stress criterion assumes failure occurs when the mean circumference stress over a critical distance next to the root of the notch tip reaches a critical value, which is expressed as,[43,44]

$$\frac{\sigma^m}{2K_{IC}}\sqrt{\pi R}=\sqrt{1+\pi R\left(\frac{f_t}{2K_{IC}}\right)^2}, \quad (1)$$

where $f_t$ is the tensile strength and can be estimated from the measured flexural strength $f_b$ by assuming the failure of the specimen follows a Weibull distribution[45] that is expressed as $f_t = f_b\,/[2(m+1)^2]^{1/m}$, in which $m$ is a Weibull shape parameter. Considering $m \approx 10$ for silica,[46] we obtain $f_t \approx 0.58 f_b$. $\sigma^m = \sigma^n \cdot K_t$, in which $\sigma^n = 3FS/2BD_R$ is the nominal maximum bending stress generated from the rupture load $F$, $B$ is the specimen thickness, $S$ is the span length between the two support pins, $D_R$ is the reduced specimen depth at the symmetric plane and is calculated as the original specimen depth minus the notch length, and $K_t$ is the stress concentration factor and is found to be ~ 2.1 based on the geometry of the notched specimens.[47] Fig. 1c shows the calculated fracture toughness $K_{IC}$ of the BNNT-silica nanocomposite of different BNNT concentrations. The fracture toughness of pure silica is found to be ~0.54 MPa·m$^{1/2}$. The addition of 0.1 wt.% BNNTs increases the fracture toughness of silica by ~54% to ~0.83 MPa·m$^{1/2}$, while the addition of 0.5 wt.% BNNTs leads to a remarkable 167% increase in fracture toughness. The substantial increases of the flexural strength and fracture toughness of the BNNT-silica nanocomposite with the introduction of a small weight percentage of BNNTs clearly show that BNNTs are an effective mechanical reinforcing filler for ceramic matrices. Notably, the property enhancement increases per unit concentration of fillers is noticeably higher for lower nanotube concentrations. The decrease in the reinforcement effectiveness at higher nanotube concentrations can be attributed to the hard-

to-avoid nanotube agglomeration inside the matrix that is more egregious at higher nanotube concentrations.[48,49]

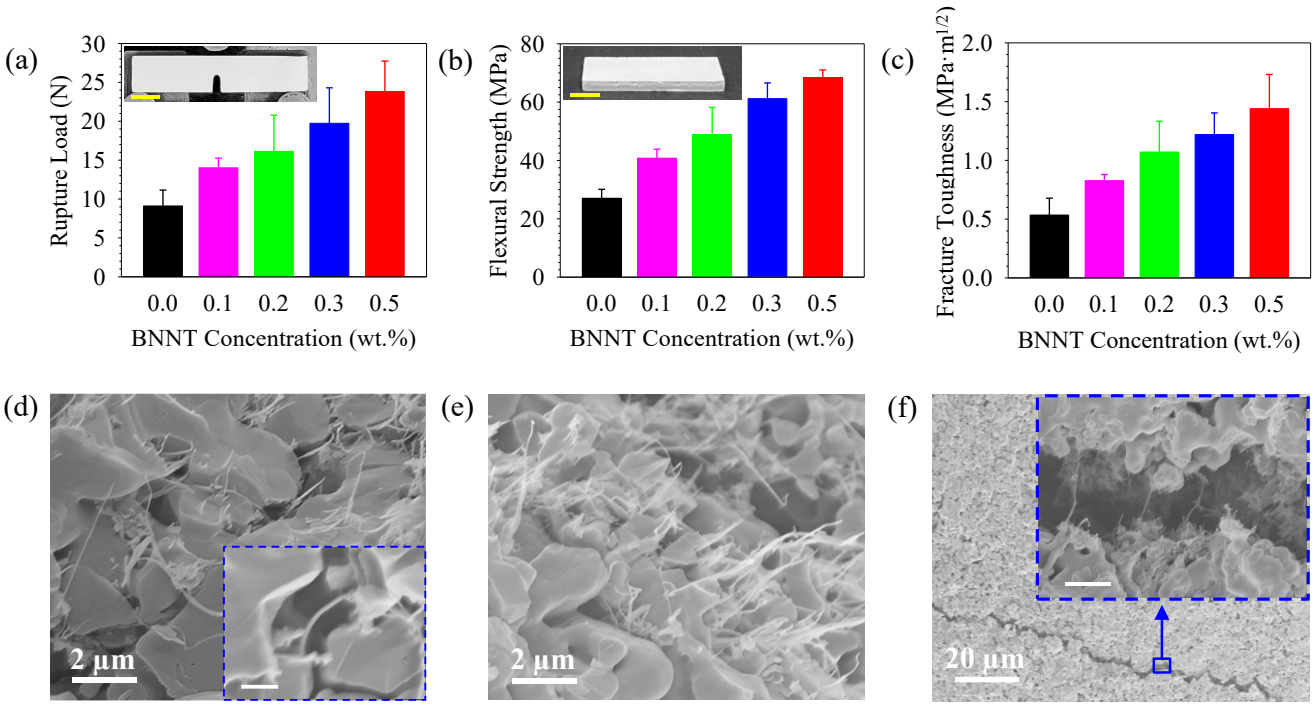


Figure 1: Mechanical Properties of BNNT-reinforced silica nanocomposites: (a) The measured rupture load (insert: one composite specimen, *scale bar* 10 mm); (b) The measured flexural strength (insert: one composite specimen, *scale bar* 5 mm); (c) The calculated fracture toughness; (d-f) SEM imaging of BNNT-silica composites: (d) BNNTs are attached to the ceramic grain surfaces and bridging grains (insert: a nanotube bridging over pores, *scale bar* 500 nm); (e) protruding BNNTs from a fractured composite surface. (f) Pulled-out nanotubes that bridge across a load-induced microcrack (insert: *scale bar* 1 µm).

Detailed SEM characterization of the nanotube conformation inside the ceramic nanocomposite was conducted to understand the failure mode and the reinforcing mechanism of the nanocomposite. Fig. 1d shows that the dispersed BNNTs are in good contact with the ceramic grain surface, with some nanotubes bridging across pores and/or multiple ceramic grains. Fig. 1e shows a number of nanotubes protruding from the ceramic matrix on the fractured surface of one tested BNNT-silica specimen. The observed nanotube pullout from the ceramic matrix, which is a major nanocomposite interface failure mode, is a clear indicator of effective interfacial load transfer on the nanotube-matrix interface,[24] and the associated friction interactions between nanotubes and matrices dissipate energy and thus increase the fracture toughness of the nanocomposite. Fig. 1f shows protruding nanotubes that bridge a micro-crack with an

opening of ~1-2 microns inside the nanocomposite, suggesting that the strong interfacial binding interactions enable the bridging BNNTs to act as crack stoppers in ceramics.

The experimentally measured flexural strength and fracture toughness improvements in BNNT-silica nanocomposites compare favorably with the literature values. For example, the measured flexural strength improvement for 0.1 wt.% BNNT-silica nanocomposites (~51%) is in good agreement with the value (~55%) reported by Sweat et al..[28] Overall, as shown in Figs. 2a and 2b, the mechanical property enhancements obtained in the present study substantially exceed those reported in the literature (see Table S1), achieving better or comparable reinforcement at much lower filler concentrations. This finding indicates that the high-purity HTP-BNNTs that are of few walls, small diameters, and up to a few hundred microns in length[39] are superior reinforcing fillers for ceramics. The bulk mechanical property enhancements reported in the present study are for composites manufactured using facile pressureless sintering techniques that offer benefits of low manufacturing cost and better manufacturability of the ceramic specimen,[50] while a majority of the studies reported in the literature[25–27,30–34] are based on composites manufactured using sophisticated pressurized sintering techniques that generally yield higher matrix densification and thus better mechanical properties.

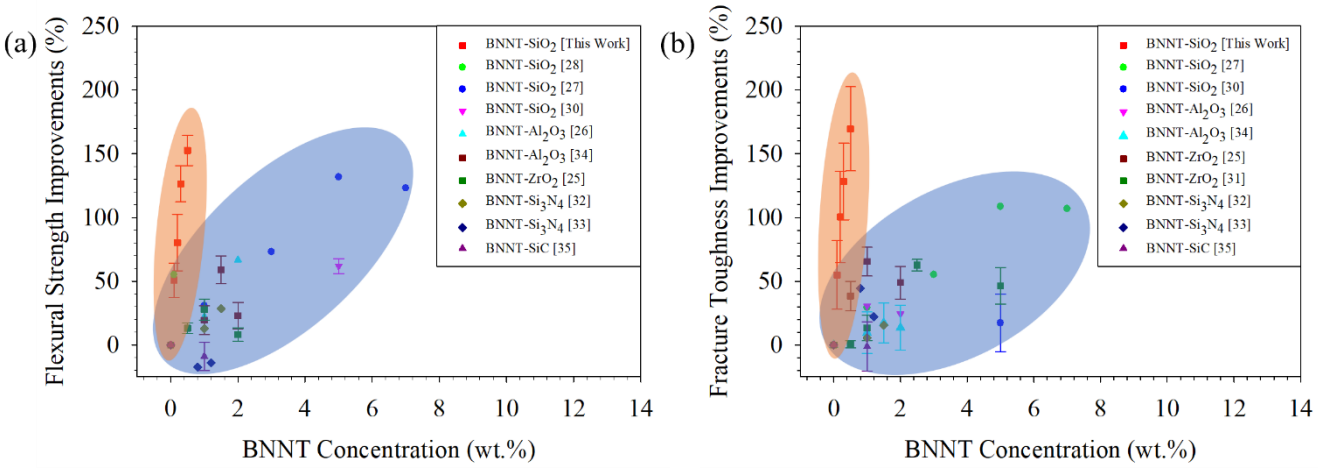


Figure 2: Comparison of our results of the bulk mechanical properties enhancement of BNNT-ceramic nanocomposites with the literature values: (a) flexural strength; (b) fracture toughness.

Table 1: Summary of the experimentally measured bulk mechanical properties of BNNT-silica ceramic composites.

| | Pure silica | 0.1% BNNT | 0.2% BNNT | 0.3% BNNT | 0.5% BNNT |
|---|---|---|---|---|---|
| **Rupture Force (**N**)** | 9.10 ± 2.0 | 14.02 ± 1.24 | 16.13 ± 4.6 | 19.73 ± 4.5 | 23.8 ± 3.9 |
| **Flexural Strength (**MPa**)** | 27.03 ± 3.0 | 40.8 ± 3.1 | 48.7 ± 9.4 | 61.2 ± 5.4 | 68.3 ± 2.7 |
| **Fracture Toughness (**MPa$\sqrt{\mathbf{m}}$**)** | 0.54 ± 0.14 | 0.83 ± 0.05 | 1.07 ± 0.26 | 1.22 ± 0.18 | 1.44 ± 0.29 |

*3.2 Interfacial load transfer characteristics of BNNT-ceramic nanocomposites*

3.2.1 *In situ* Raman micromechanical characterization

*In situ* Raman measurements were conducted to investigate the interfacial load transfer characteristics, providing insights into the local stress and strain evolution in the fracture response. The Raman spectrum of BNNTs, as displayed in Fig. 3a, shows a characteristic peak of its active $E_{2g}$ band at ~1369 $cm^{-1}$,[51,52] which is sensitive to strain in response to the length change of the B-N bond.[53] Therefore, it is feasible to assess the mechanical straining of BNNTs inside nanocomposites by measuring the peak frequency change of its signature Raman band. Because of their large electronic bandgap properties and the resulting non-resonant Raman scattering of lights, the Raman peak intensity of BNNTs is generally weak.[54] Our studies show that the Raman band of BNNTs in sintered BNNT-silica is hard to measure precisely because of its low intensity at low nanotube concentrations. This study only reports the data based on Raman measurements of 0.5 wt.% BNNT-silica with a distinguishable Raman band and a reasonably strong Raman peak intensity, as exemplified by the two selected Raman spectra (black and red curves) shown in Fig. 3a. A down-shift of the BNNT's Raman peak frequency to ~1367 $cm^{-1}$ is observed for the unsintered nanocomposite, indicating that nanotubes were subjected to tension in the nanocomposite. After sintering, the BNNT's Raman peak frequency is found to shift upward to ~1370 $cm^{-1}$, suggesting that nanotubes are under compression within the ceramic matrix. That can be attributed to the shrinkage of the silica matrix during the densification process, which compresses the nanotubes. The 2D Raman mapping of an area of 300 μm by 300 μm at a spatial interval of 7.3 μm, as displayed in Fig. 3b, shows that nanotubes are mostly under compression with Raman peak frequency within 1369-1371 $cm^{-1}$, while BNNTs experience tension at only a few sporadic locations with Raman peak frequency within 1367-1369 $cm^{-1}$.

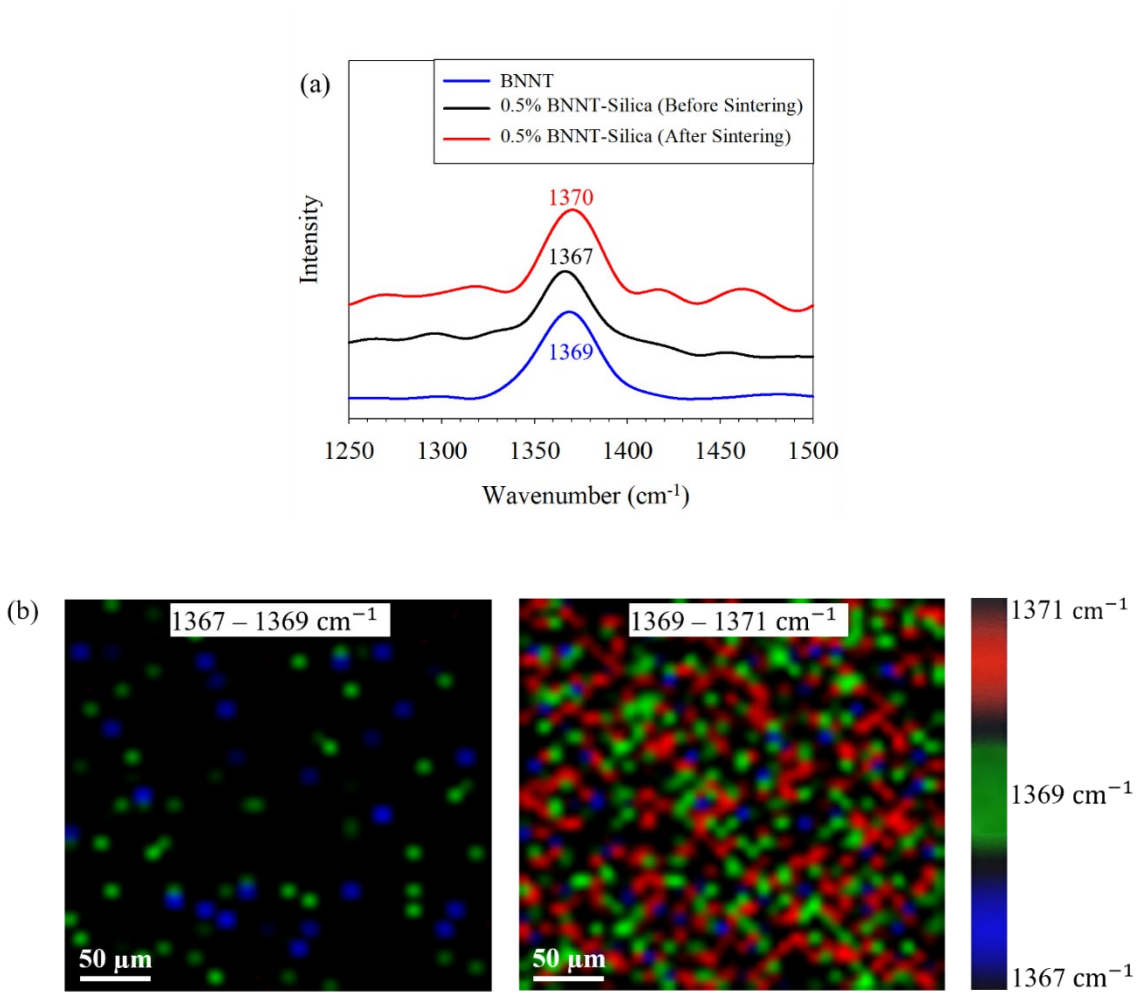


Figure 3: Raman Characterization of BNNT-reinforced silica nanocomposites: (a) Comparison of the Raman spectra of pure BNNTs (blue) and 0.5 wt.% BNNT-silica before (black) and after (red) sintering. (b) 2D Raman mapping of the BNNT's characteristic band peak frequency inside the composite.

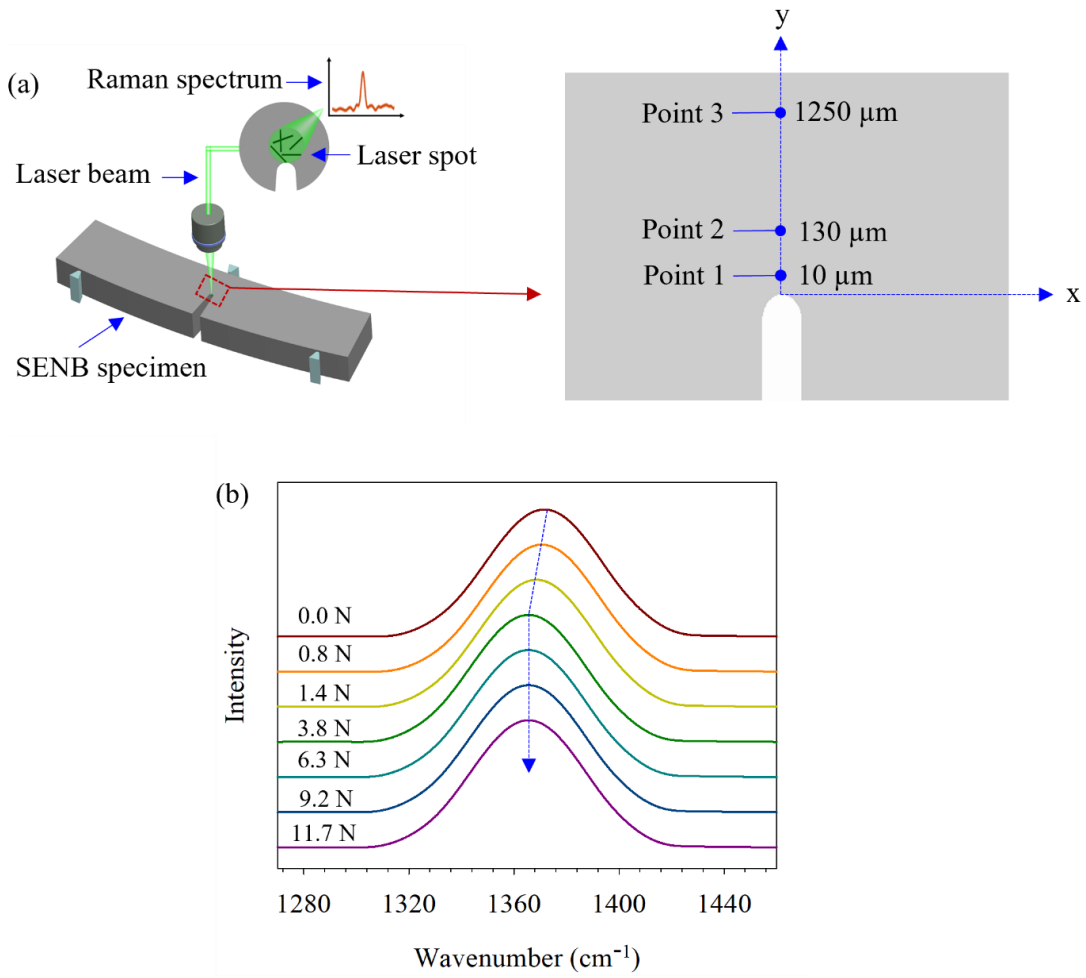


Figure 4: *In situ* Raman micromechanical characterization of BNNT-reinforced silica nanocomposites. (a) Schematic drawings of the measurement setup and the specimen near the notch root tip (not to scale); (b) Selected Raman spectra of BNNTs under various loads.

Fig. 4a illustrates the *in-situ* Raman micromechanical measurement performed on a BNNT-silica SENB specimen. In this experiment, for every 10-μm displacement of the loading pin, Raman spectra were recorded at three selected locations along the symmetric plane, which are of a respective distance of ~10 μm (Point 1), ~130 μm (Point 2), and ~1.3 mm (Point 3) from the notch root tip. Fig. 4b shows selected Raman spectra of BNNTs near the notch root tip (Point 1) during the three-point bending measurement. The BNNT's Raman peak shifts downward after the load is applied, and this downward shift continues till a loading displacement of 30 μm (3.8 N). The downward peak shifts indicate that the nanotubes experience tensile strain near the crack tip during loading, which is attributed to the shear load transferred along the nanotube-matrix interface. With further increases of the loading displacement up to the fracture

of the specimen, the Raman peak shift is found to remain relatively unchanged, indicating that the effective interfacial load transfer between nanotubes and the matrix reaches a saturated level, and slippage occurs on the nanotube-matrix interface. The spot of the laser beam employed in our measurement is about 1.2 μm in diameter, and the observed Raman peak frequency shift represents the collective average straining of the nanotubes inside the interactive volume of the laser beam with the nanocomposite.[49] The left-column plots in Fig. 5 show the Raman peak frequency change as a function of the measured applied load at those three selected locations. The results show that the Raman peak frequency at Point 1 first downshifts nearly linearly with the applied load up to ~2 N and then reaches a saturated level up to fracture with a total peak frequency shift of ~1.1 $cm^{-1}$. A similar trend is also observed for the Raman peak frequency change at Point 2, with the peak frequency saturated at a load of ~5 N and a total peak frequency shift of ~1.1 $cm^{-1}$. The results show the shear-lag effect in the interfacial stress transfer, which has been observed in nanotube-reinforced polymer nanocomposites.[48,49] In contrast, little Raman peak frequency change is observed at Point 3. The results show that nanotubes at Point 1 are strained ahead of those at Point 2, but both experience a similar level of maximum tensile strains, while nanotubes at Point 3 are not noticeably strained. Overall, the Raman analysis reveals that those nanotubes near the notch tip are under higher levels of tensile straining, thus contributing more to the improvement of the bulk mechanical properties.

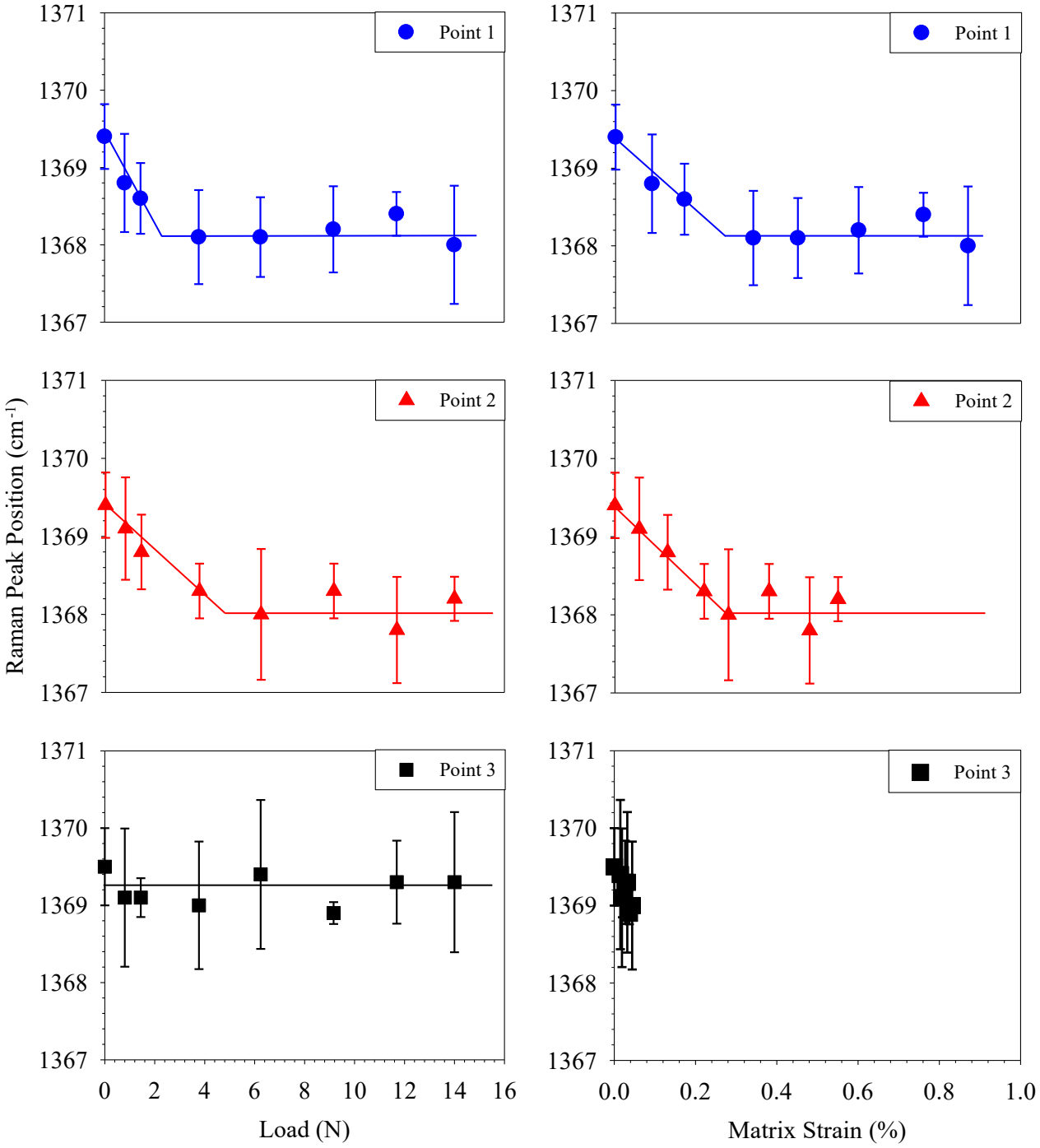


Figure 5: Representative *in situ* Raman micromechanical measurements (dots) at three selected spots near the notch tip of a 0.5 wt.% BNNT-silica specimen. The solid lines are the respective fitting curves.

3.2.2 Characterization of local deformations and interfacial load transfer

The straining of nanotubes inside the nanocomposite is caused by the shear load transferred along the nanotube-matrix interface. Before the onset of interfacial slippage, the strain in the nanotubes equals the strain in the matrix that is in direct contact with the nanotubes. Here we use the digital image correlation or DIC technique, in conjunction with finite element method (FEM) simulations (see Fig. S3), to directly quantify the local deformation of the matrix, in particular, the critical strain in the matrix at the onset of interfacial slippage. The strain in the SENB specimen along the symmetric plane is dominant in the longitudinal- or *x*-direction (Fig. 4a).

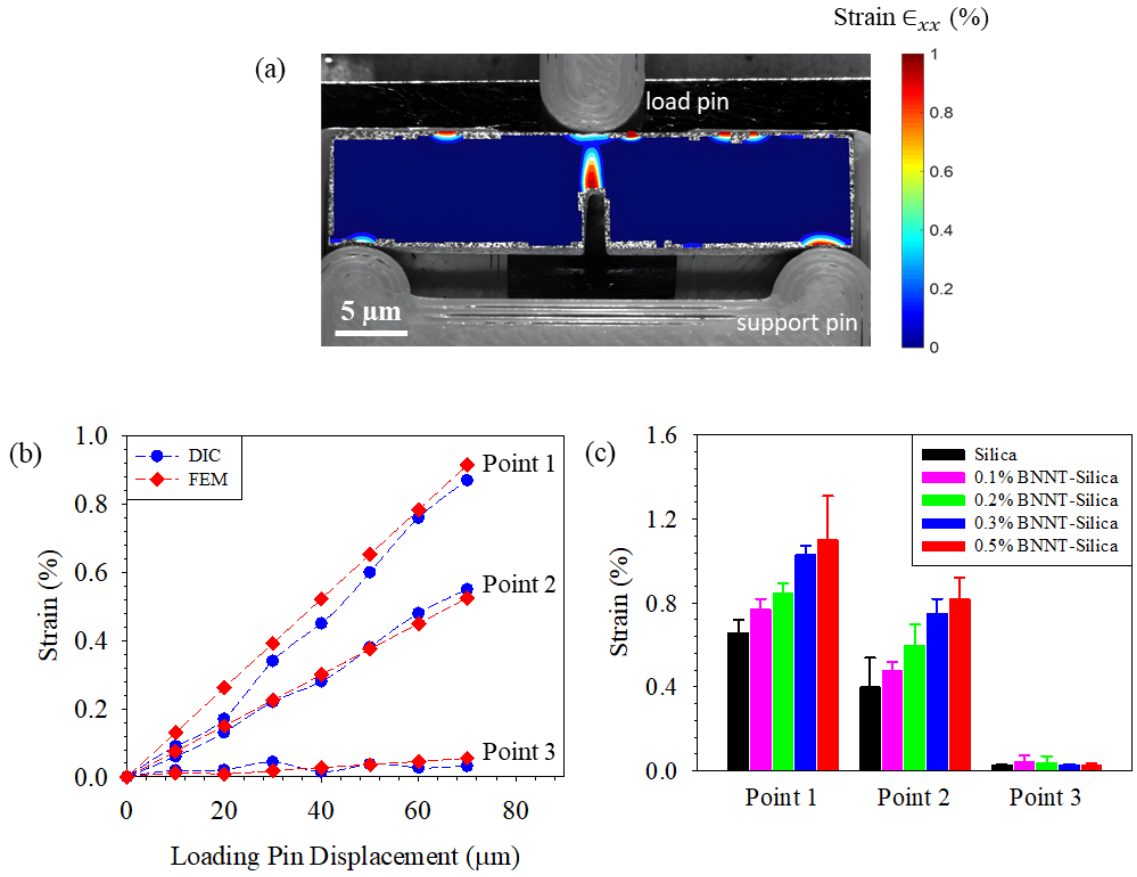


Figure 6: Experimental characterization of the local deformations of BNNT-silica nanocomposites using digital image correlation (DIC) techniques: (a) Selected DIC strain map overlaid on the optical image of the test specimen; (b) The comparison between the DIC-measured strain and the FEM-predicted strain at three selected points. (c) The measured DIC strains under failure loads for nanocomposite specimens.

Fig. 6a shows a typical DIC map of the *x*-axis normal strain in the matrix, which overlays the corresponding optical image of one notched 0.5 wt.% BNNT-silica specimen that was recorded right before the onset of fracture. Fig. 6b shows a generally good agreement between the DIC-measured and FEM-predicted *x*-axis normal strains at those three selected spots as shown in Fig.4a, which manifests the validity and accuracy of our DIC strain measurements. Fig. 6c shows the matrix's normal strain at those three selected spots under fracture load. The results show that a substantial failure strain increase from ~0.66% to ~1.11% is observed at Point 1 with the BNNT concentration increasing from 0 to 0.5 wt.%, while little change is observed at Point 3. The measured load-strain relationship allows the conversion of the Raman peak frequency shift versus load relationships (Fig. 5, left column) to the Raman peak frequency shift versus matrix strain relationships, which are exhibited in Fig. 5, right column. Our analysis shows that the critical matrix strain in 0.5 wt.% BNNT-silica at the onset of interfacial slippage is ~0.27%.

The nanotubes in the manufactured BNNT-silica nanocomposite are expected to be oriented randomly, which is confirmed by polarized Raman microscopy measurements (Fig. S4). Therefore, the actual strain of the nanotubes inside the nanocomposite is smaller than the matrix strain. For a simplified 2D nanotube nanocomposite system as illustrated in Fig. 7a, the strain in a nanotube $\epsilon_{nt}$ is given as $\epsilon_{nt} = \epsilon_x(cos^2\theta - v_m sin^2\theta)$, where $v_m$ is the Poisson's ratio of the matrix and $\theta$ is the nanotube alignment angle with respect to the tensile force direction (i.e., *x*-axis). In a fully random nanotube composite system, the collective average nanotube strain is given as

$$\epsilon_{nt}^{ave} = \frac{2}{\pi}\int_0^{\pi/2} \epsilon_x(cos^2\theta - v_m sin^2\theta)d\theta = \frac{1-v_m}{2}\epsilon_x. \quad (2)$$

Eqn. 2 shows the average nanotube strain equals the strain of those nanotubes oriented 45° from the matrix's stretching direction. The actual critical nanotube strain corresponding to the onset of interfacial slippage is calculated to be ~0.11% based on Eqn. 2 by assuming $v_m = 0.17$.[55] This result indicates that the normal stress in the nanotube reaches a saturated level of ~1.2 GPa at the onset of interfacial slippage by considering Young's modulus $E_{nt}$=1.07 TPa for HTP-BNNTs.[11]

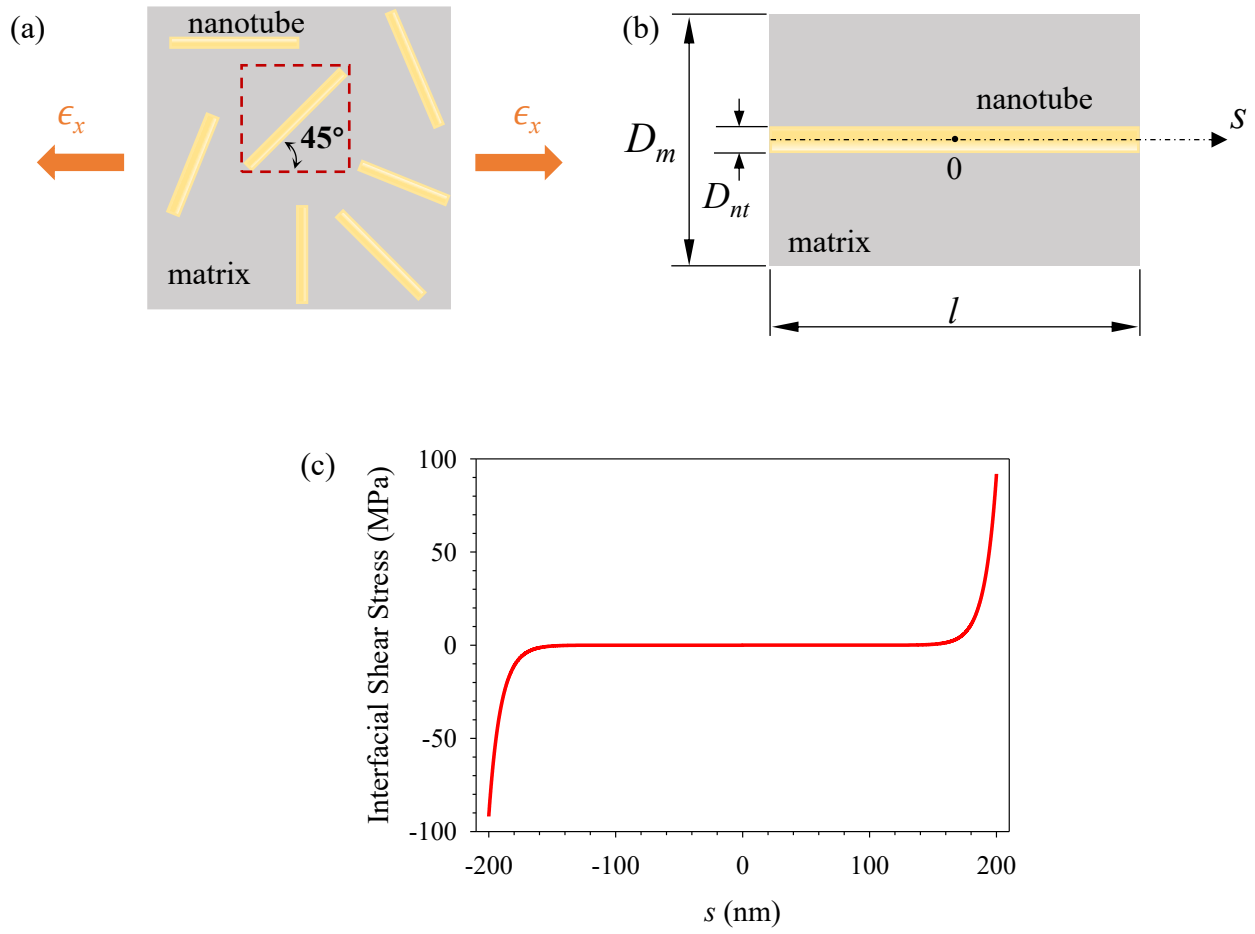


Figure 7: (a) A simplified 2D schematics of nanotube-reinforced nanocomposites. (b) Schematic of a cylindrical-shaped single nanotube nanocomposite. (c) The pointwise interfacial shear stress distribution along the BNNT-silica interface.

As discussed in Section 3.2.1, *in-situ* Raman measurements indicate that the interfacial shear transfer inside the BNNT-silica nanocomposite follows a shear-lag behavior. For a sufficiently long and straight nanotube of diameter $D_{nt}$ inside a cylindrical matrix of diameter $D_m$ as illustrated in Fig. 7b, the pointwise interfacial shear stress distribution along the nanotube surface $\tau$ is given as[49]

$$\tau = \frac{E_{nt}\,\epsilon_{nt}}{2}\frac{\cosh(2n\cdot s/D_{nt})}{\sinh(n\cdot l/D_{nt})}, \tag{3}$$

where $s$ is the coordinate along the longitudinal direction of the nanotube, $l$ is the length of the nanotube, $n = \sqrt{\frac{E_m}{E_{nt}\cdot(1+\nu_m)\cdot\log\left(\frac{D_m}{D_{nt}}\right)}}$, in which $E_m$ is the Young's modulus of the matrix. The maximum interfacial shear stress occurs at the two ends of the nanotube (i.e., $s = \pm\, l\,/2$) and is calculated to be ~92 MPa at the

onset of interfacial slippage (i.e., $\epsilon_{nt} = 0.11\%$) for 0.5 wt.% BNNT-silica. The pointwise interfacial shear stress distribution profile is shown in Fig. 7c. The following parameters are used in the calculation: $E_m =$ 70 GPa;[56] $D_{nt} = 2.9\ nm$; $D_m$ = 31.3 nm that is calculated based on the densities of silica (2.3 g/cm$^3$) and BNNTs (1.35 g/cm$^3$); $l$ = 400 nm. Our analysis shows that the maximum shear stress is independent of the nanotube length $l$ when $l$ > 72 nm. The maximum interfacial stress obtained here is one order of magnitude smaller than the value (~1.25 GPa) obtained from our recent *in situ* SEM nanomechanical single nanotube pullout measurements.[24] Single-nanotube pullout measurements were conducted on nearly perfect interfaces formed by individual straight BNNTs and the silica matrix. The interfaces are free of many hard-to-avoid processing-induced nonidealities in bulk nanotube nanocomposites (e.g., nanotube bundling, networking, waviness and misalignment). The much lower interfacial stress in the bulk BNNT-silica nanocomposite results in a substantially lower reinforcing efficiency of BNNTs. The findings indicate there is plenty of room for further bulk properties enhancement for BNNT-ceramic nanocomposites, should the interfacial load transfer be improved by minimizing those processing-induced nanotube nonidealities.

3.2.3 Influence of the Interfacial Load Transfer on the Bulk Flexural Strength

The quantified interfacial load transfer characteristics in Section 3.2.2 enable the assessment of the contribution of the interfacial load transfer to the bulk mechanical properties, such as flexural strength, of the BNNT-silica composite. For the single-nanotube composite as shown in Fig. 7b, its tensile strength is given as $f_t = f_t^m(1 - V_{nt}) + \sigma_{nt}V_{nt}$ based on the rule of mixtures, where $f_t^m$ is the tensile strength of the matrix, $\sigma_{nt}$ is the saturated tensile stress in the nanotube at the onset of the interfacial slippage, and $V_{nt}$ is the volume fraction of the nanotube. For 0.5 wt.% BNNT-silica composites, we have $f_t^m \approx 15.67$ MPa by assuming $f_t \approx 0.58 f_b$ (see Section 3.1); $\sigma_{nt}$ = 1.2 GPa; $V_{nt}$ = 0.85%. These parameters yield a tensile/flexural strength enhancement of ~64%, which, however, is significantly below the experimentally measured enhancement of ~154%. This observation of extra strengthening beyond the rule of mixtures prediction indicates that the measured bulk mechanical property enhancements of BNNT-silica may not be fully attributed to the effective interfacial load transfer. The microstructural changes caused by the incorporation of BNNTs likely substantially enhance the matrix's properties, thus the bulk properties of the composite,[27] with a contribution level comparable to, or even exceeding, that of the interfacial load transfer. The substantial contribution of the microstructural changes revealed here is in part because of the relatively low reinforcing efficiency from the interfacial load transfer, resulting in a transferred nanotube stress (~1.2 GPa) only a small fraction of the ultimate stress level (~30.2 GPa) obtained from single-nanotube pullout measurements.[14,24] Therefore, the strengthening of the ceramic by the interfacial load

transfer remains a primary reinforcing factor, provided the interfacial load transfer on the nanotube-matrix interface can be at least modestly improved. Even though the effect of the added BNNTs on the composite's bulk mechanical properties via the induced microstructure change has been reported qualitatively in prior studies,[26,27] this study is among the first to provide a more quantitative assessment of this effect. The established experimental-theoretical framework can be readily extended to other nanofiber-reinforced nanocomposites to assess the respective contributions of the interfacial load transfer and the microstructural changes toward the bulk property enhancement.

### *3.3 Microstructural Characteristics of BNNT-ceramic composites*

In this section, we investigate the microstructural characteristics of BNNT-silica nanocomposites, focusing on the microstructural change of the matrix caused by the incorporation of BNNTs.

#### 3.3.1 Densification and porosity

Fig. 8a shows the porosity of sintered BNNT-silica specimens based on the density measurement using the Archimedes method.[57] The results show that the pure silica specimen possesses a porosity of ~1% and increases with the BNNT concentration. The porosity of 0.5 wt.% BNNT-silica reaches ~4%. X-ray measurements, as exemplified in Fig. 8b, show that the sintered BNNT-silica nanocomposite specimen possesses a rather uniform densification without any sizeable internal cracks. We performed detailed SEM imaging of polished pure silica and BNNT-silica nanocomposite specimens. The results shown in Figs. 8c and 8d confirm that the specimens possess overall uniform densification, which is consistent with our EDX results (Fig. S5). The pure silica specimen is shown to contain small sub-micron pores (zoom-in view in Fig. 8c). In contrast, the 0.5 wt.% nanocomposite specimen is featured with larger pores with size reaching up to 2 microns (zoom-in view in Fig. 8d). The formation of larger pores in BNNT-silica may be attributed to the enlarged gaps between ceramic particles caused by the nanotube aggregation and trapped materials (e.g., nanotube impurities) and moisture, which could be mitigated by using high-vacuum and/or pressurized sintering techniques. The findings about the pore size are consistent with our density-based porosity measurement. In brief, the addition of BNNTs noticeably increases the porosity of silica.

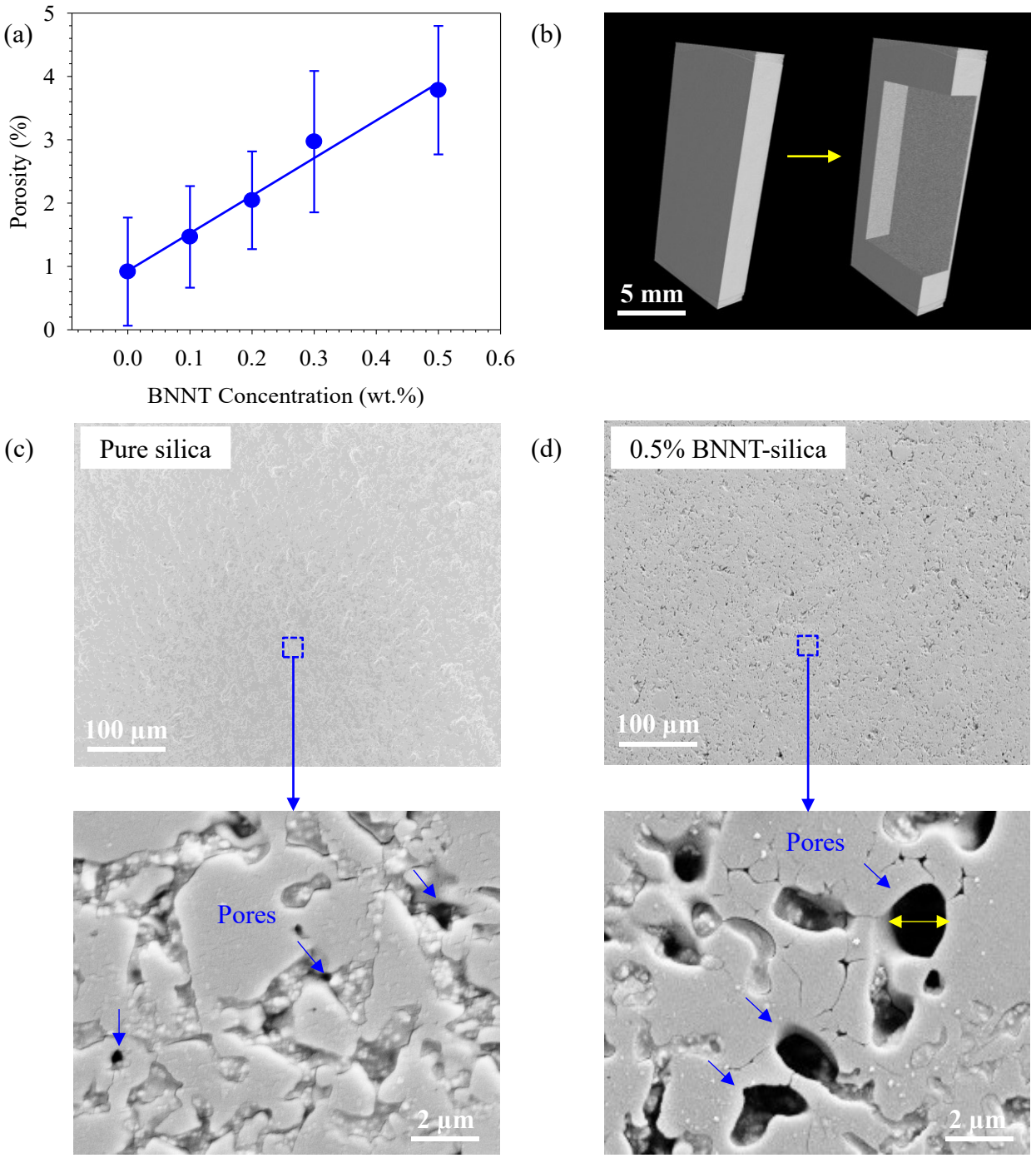


Figure 8: Densification and Porosity of BNNT-reinforced silica nanocomposites: (a) The measured porosity of pure silica and BNNT-silica nanocomposites. (b) 3D X-ray image showing that the composite specimen possesses uniform densification and is free of noticeable cracks. (c-d) SEM images of the polished surface morphology of (c) pure silica and (d) 0.5 wt.% BNNT-silica nanocomposites and typical zoom-in views (bottom).

3.3.2 Matrix crystallinity

Fig. 9a compares the XRD patterns of as-received silica powders, sintered silica, and 0.5 wt.% BNNT-silica nanocomposite samples. The distinct peaks at 20.8° and 26.6° for silica powders show the presence of quartz in the as-received powder because the employed silica powder of 1 μm in size is polycrystalline quartz, while the smaller powder of 20-30 nm in size is amorphous silica. After sintering, cristobalite peaks are observed at around 21.9°, indicating the formation of cristobalite crystals during the sintering process. A decreasing trend of the quartz peaks with increasing BNNT concentration is also observed. Meanwhile, the XRD peak intensity of cristobalite in the BNNT-silica nanocomposite is notably higher than that in pure silica. The analysis of XRD peak ratios, particularly those of the dominant cristobalite peak at 21.9° and the quartz peak at 26.6°, reveals an increasing trend with the BNNT concentration, as shown in Fig. 9b. This trend indicates an augmentation in cristobalite crystallization with BNNTs acting

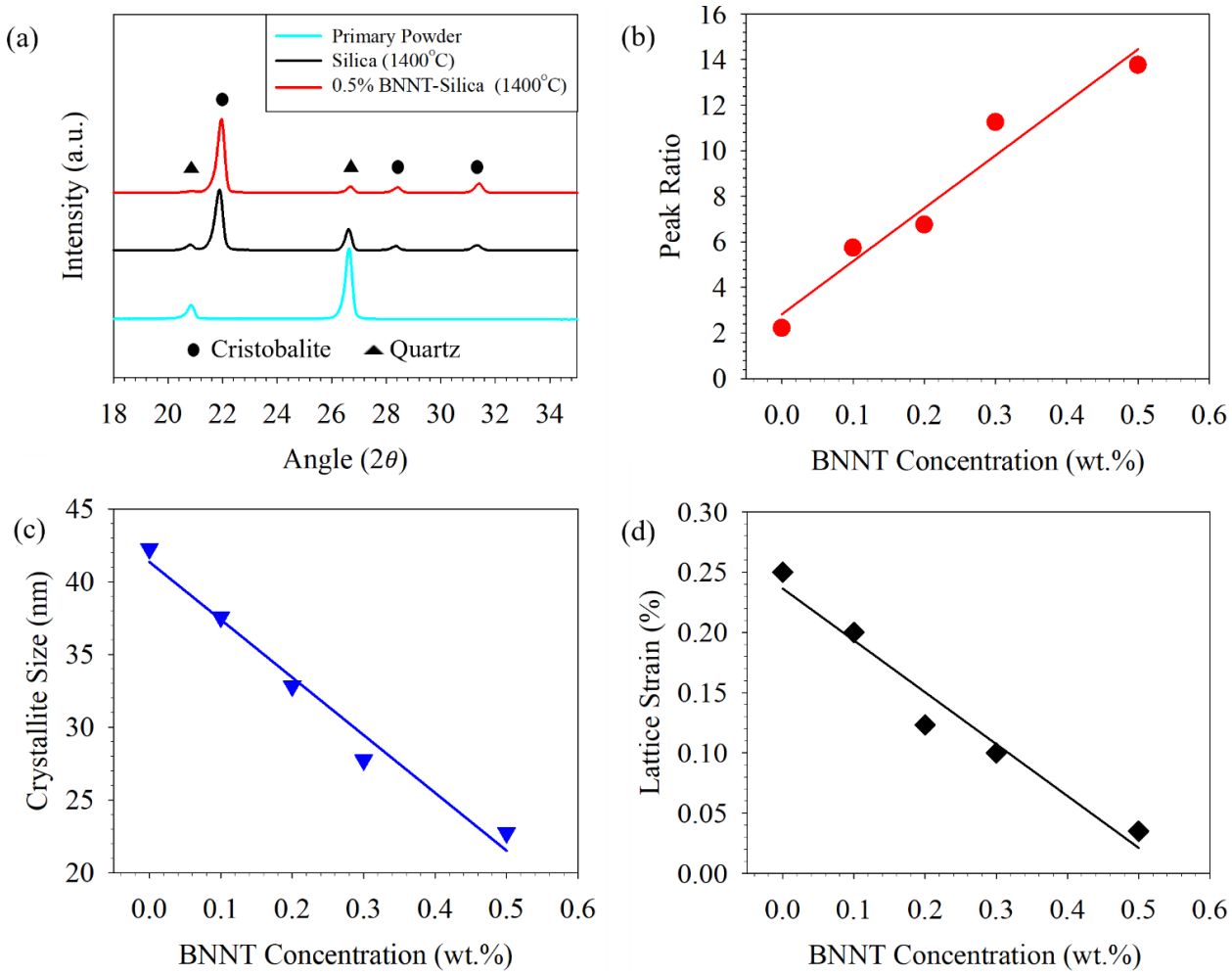


Figure 9: Crystallinity of BNNT-reinforced silica nanocomposites: (a) XRD patterns of as-received silica powder, pure silica and 0.5% BNNT-silica samples sintered at 1400°C; (b-d) Cristobalite to quartz peak ratio (b); crystallite size (c) and lattice strain (d).

as a nucleating agent.[58,59] These findings underscore the influential role of BNNTs in the crystallization of silica, which reportedly improves its mechanical properties.[60]

The lattice spacing of α-cristobalites ($d_{101\alpha}$) for silica decreases with the addition of BNNTs. Lattice spacing $d_{101\alpha}$ is found to be 0.4069 ± 0.0001 nm for pure silica, and changes into 0.4056 ± 0.0002 nm (0.1 wt.%), 0.4058nm ± 0.0001 (0.2 wt.%), 0.4053 ± 0.0001 nm (0.3 wt.%) and 0.4055 ± 0.0002 nm (0.5 wt%) for BNNT-silica. While the lattice spacing of BNNT-silica appears insensitive to the nanotube concentration, the presence of BNNTs noticeably decreases the lattice spacing of cristobalite compared to pure silica. This alteration in lattice spacing can be attributed to changes in lattice strain caused by the contracting phase transformation of $\alpha$-cristobalite during the sample cooling process.[61] Figs 9c and 9d show the crystallite size and the lattice strain as a function of the BNNT concentration, respectively. Here, the crystallite size and the lattice strain are calculated by using the Williamson-Hall method[62] in the $2\theta$ range of 18-70°. The dependence of the intensity and broadening of the diffraction peaks on the crystallite size and lattice strain is given as

$$\beta cos\theta = \frac{K\lambda}{D} + 2\epsilon_l sin\theta \tag{4}$$

where $\beta$ is the full width at half maximum of the XRD peak, $\theta$ is the Bragg angle, $K$ is Scherer constant (generally $K \approx 0.9$), $\lambda$ is the X-ray wavelength ($\lambda$ = 1.5406 Å for Cu Kα radiation), $D$ is the crystallite size, and $\epsilon_l$ is the lattice strain. The crystallite size is determined to be about 42.3 nm for pure silica and follows a decreasing trend with an increase of the BNNT concentration (Fig. 9c). The reduction in crystallite size may have a profound impact on the material's mechanical properties, including increased strength and toughness. The lattice strain, as shown in Fig. 9d, decreases with an increase in the BNNT concentration, implying that the added BNNTs reduce the lattice structural distortion. The decreases in the lattice strain and structural distortion enhance the bulk mechanical properties.[63]

In summary, the observed microstructural changes in BNNT-silica nanocomposites have a mixed influence on their bulk mechanical properties. On one hand, the increased pore size and porosity decrease the mechanical properties as micropores act as stress concentration sites where cracks nucleate. On the other hand, the decrease in the crystalline grain size and the lattice strain leads to the strengthening of the ceramic matrix. Nonetheless, the observed substantial mechanical strengthening in BNNT-silica nanocomposites indicates the reinforcing roles of BNNTs in ceramics through effective interface load transfers and collective microstructural influences. Mitigating the porosity issue by improving the manufacturing process (e.g., by using high-vacuum and/or pressurized sintering techniques) could open new avenues to further improve the mechanical reinforcement of nanotube-ceramic nanocomposites.

## 4. Conclusion

The enhancement of the bulk mechanical properties of BNNT-reinforced silica nanocomposites was experimentally investigated. The studies reveal a substantial increase in flexural strength and fracture toughness with the introduction of a small amount of BNNTs. The interfacial stress transfer in bulk BNNT-silica nanocomposite exhibits a shear-lag behavior. Slippage on the nanotube-matrix interface occurs before the failure of the matrix. The nanotube pullout and the resulting nanotube bridging across microcracks are the major strengthening and toughening mechanisms. The incorporation of BNNTs noticeably changes the porosity and crystallinity of the underlying ceramic matrix. The results reveal that the effective interfacial load transfer and the collective influence of the microstructural changes contribute to the remarkable bulk mechanical property enhancement, rendering BNNTs a superior reinforcing filler for ceramics. The findings are useful for a better understanding of the reinforcement of nanotubes in ceramics and contribute to the development of light, strong, tough, and durable ceramic materials.

**Supporting information** contains additional details about the employed nanotube materials, the tested composite specimens, mechanical testing methods, and nanotube alignment and distribution inside the composite specimen, pore size distribution, and literature data on the BNNT-ceramic composite.


## Acknowledgments

The authors acknowledge the support of the National Science Foundation under grant no. CMMI 2009134.


## Conflict of Interest

The authors declare that they have no conflict of interest.

## References:


(1) Rubio, A.; Corkill, J. L.; Cohen, M. L. Theory of Graphitic Boron-Nitride Nanotubes. *Physical Review B* **1994**, *49* (7), 5081–5084.

(2) Chopra, N. G.; Luyken, R. J.; Cherrey, K.; Crespi, V. H.; Cohen, M. L.; Louie, S. G.; Zettl, A. Boron-Nitride Nanotubes. *Science* **1995**, *269* (5226), 966–967.

(3) Kundalwal, S. I.; Choyal, V. K.; Luhadiya, N.; Choyal, V. Effect of Carbon Doping on Electromechanical Response of Boron Nitride Nanosheets. *Nanotechnology* **2020**, *31* (40), 405710. https://doi.org/10.1088/1361-6528/ab9d43.

(4) Gupta, M.; Meguid, S. A.; Kundalwal, S. I. Synergistic Effect of Surface-Flexoelectricity on Electromechanical Response of BN-Based Nanobeam. *Int J Mech Mater Des* **2022**, *18* (1), 3–19. https://doi.org/10.1007/s10999-021-09582-6.

(5) Treacy, M. M. J.; Ebbesen, T. W.; Gibson, J. M. Exceptionally High Young's Modulus Observed for Individual Carbon Nanotubes. *Nature* **1996**, *381* (6584), 678–680. https://doi.org/10.1038/381678a0.

(6) Chopra, N. G.; Zettl, A. Measurement of the Elastic Modulus of a Multi-Wall Boron Nitride Nanotube. *Solid State Commun.* **1998**, *105* (5), 297–300.

(7) Arenal, R.; Wang, M.-S.; Xu, Z.; Loiseau, A.; Golberg, D. Young Modulus, Mechanical and Electrical Properties of Isolated Individual and Bundled Single-Walled Boron Nitride Nanotubes. *Nanotechnology* **2011**, *22* (26), 265704. https://doi.org/10.1088/0957-4484/22/26/265704.

(8) Hernandez, E.; Goze, C.; Bernier, P.; Rubio, A. Elastic Properties of C and BxCyNz Composite Nanotubes. *Physical Review Letters* **1998**, *80* (20), 4502–4505.

(9) Choyal, V.; Choyal, V. K.; Kundalwal, S. I. Effect of Atom Vacancies on Elastic and Electronic Properties of Transversely Isotropic Boron Nitride Nanotubes: A Comprehensive Computational Study. *Computational Materials Science* **2019**, *156*, 332–345. https://doi.org/10.1016/j.commatsci.2018.10.013.

(10) Suryavanshi, A. P.; Yu, M.-F.; Wen, J.; Tang, C.; Bando, Y. Elastic Modulus and Resonance Behavior of Boron Nitride Nanotubes. *Applied Physics Letters* **2004**, *84* (14), 2527–2529. https://doi.org/10.1063/1.1691189.

(11) Zhao, Y.; Chen, X.; Park, C.; Fay, C. C.; Stupkiewicz, S.; Ke, C. Mechanical Deformations of Boron Nitride Nanotubes in Crossed Junctions. *J Appl. Phys.* **2014**, *115* (16), 164305. https://doi.org/10.1063/1.4872238.

(12) Zheng, M.; Chen, X.; Park, C.; Fay, C. C.; Pugno, N. M.; Ke, C. Nanomechanical Cutting of Boron Nitride Nanotubes by Atomic Force Microscopy. *Nanotechnology* **2013**, *24* (50), 505719. https://doi.org/10.1088/0957-4484/24/50/505719.

(13) Wei, X.; Wang, M.-S.; Bando, Y.; Golberg, D. Tensile Tests on Individual Multi-Walled Boron Nitride Nanotubes. *Adv. Mater.* **2010**, *22* (43), 4895–4899. https://doi.org/10.1002/adma.201001829.

(14) Jiang, Y.; Li, N.; Liu, Z.; Yi, C.; Zhou, H.; Park, C.; Fay, C. C.; Deng, J.; Chew, H. B.; Ke, C. Exceptionally Strong Boron Nitride Nanotube Aluminum Composite Interfaces. *Extreme Mechanics Letters* **2023**, *59*, 101952. https://doi.org/10.1016/j.eml.2022.101952.

(15) Qu, W.; Bagchi, S.; Chen, X.; Chew, H. B.; Ke, C. Bending and Interlayer Shear Moduli of Ultrathin Boron Nitride Nanosheet. *J. Phys. D: Appl. Phys.* **2019**, *52* (46), 465301. https://doi.org/10.1088/1361-6463/ab3953.

(16) Garel, J.; Leven, I.; Zhi, C.; Nagapriya, K. S.; Popovitz-Biro, R.; Golberg, D.; Bando, Y.; Hod, O.; Joselevich, E. Ultrahigh Torsional Stiffness and Strength of Boron Nitride Nanotubes. *Nano Lett.* **2012**, *12* (12), 6347–6352. https://doi.org/10.1021/nl303601d.

(17) Zheng, M.; Chen, X.; Bae, I.-T.; Ke, C.; Park, C.; Smith, M. W.; Jordan, K. Radial Mechanical Properties of Single-Walled Boron Nitride Nanotubes. *Small* **2012**, *8* (1), 116–121. https://doi.org/10.1002/smll.201100946.

(18) Zheng, M.; Zou, L.-F.; Wang, H.; Park, C.; Ke, C. Engineering Radial Deformations in Single-Walled Carbon and Boron Nitride Nanotubes Using Ultrathin Nanomembranes. *ACS Nano* **2012**, *6* (2), 1814–1822. https://doi.org/10.1021/nn2048813.

(19) Zheng, M.; Ke, C.; Bae, I.-T.; Park, C.; Smith, M. W.; Jordan, K. Radial Elasticity of Multi-Walled Boron Nitride Nanotubes. *Nanotechnology* **2012**, *23* (9), 095703. https://doi.org/10.1088/0957-4484/23/9/095703.

(20) Lei, H.; Shi, Q.; Chen, J. Research on BNNTs/Epoxy/Silicone Ternary Composite Systems for High Thermal Conductivity. *IOP Conf. Ser.: Mater. Sci. Eng.* **2018**, *381* (1), 012076. https://doi.org/10.1088/1757-899X/381/1/012076.

(21) Chen, X.; Dmuchowski, C. M.; Park, C.; Fay, C. C.; Ke, C. Quantitative Characterization of Structural and Mechanical Properties of Boron Nitride Nanotubes in High Temperature Environments. *Scientific Reports* **2017**, *7* (1), 11388. https://doi.org/10.1038/s41598-017-11795-9.

(22) Tank, M. J.; Reyes, A. N.; Park, J. G.; Scammell, L. R.; Smith, M. W.; De Leon, A.; Sweat, R. D. Extreme Thermal Stability and Dissociation Mechanisms of Purified Boron Nitride Nanotubes: Implications for High-Temperature Nanocomposites. *ACS Appl. Nano Mater.* **2022**, *5* (9), 12444–12453. https://doi.org/10.1021/acsanm.2c01965.

(23) Li, N.; Dmuchowski, C. M.; Jiang, Y.; Yi, C.; Gou, F.; Deng, J.; Ke, C.; Chew, H. B. Sliding Energy Landscape Governs Interfacial Failure of Nanotube-Reinforced Ceramic Nanocomposites. *Scripta Materialia* **2022**, *210*, 114413. https://doi.org/10.1016/j.scriptamat.2021.114413.

(24) Yi, C.; Bagchi, S.; Gou, F.; Dmuchowski, C. M.; Park, C.; Fay, C. C.; Chew, H. B.; Ke, C. Direct Nanomechanical Measurements of Boron Nitride Nanotube—Ceramic Interfaces. *Nanotechnology* **2019**, *30* (2), 025706. https://doi.org/10.1088/1361-6528/aae874.

(25) Xu, J.-J.; Bai, Y.-J.; Wang, W.-L.; Wang, S.-R.; Han, F.-D.; Qi, Y.-X.; Bi, J.-Q. Toughening and Reinforcing Zirconia Ceramics by Introducing Boron Nitride Nanotubes. *Materials Science and Engineering: A* **2012**, *546*, 301–306. https://doi.org/10.1016/j.msea.2012.03.077.

(26) Wang, W.-L.; Bi, J.-Q.; Wang, S.-R.; Sun, K.-N.; Du, M.; Long, N.-N.; Bai, Y.-J. Microstructure and Mechanical Properties of Alumina Ceramics Reinforced by Boron Nitride Nanotubes. *Journal of the European Ceramic Society* **2011**, *31* (13), 2277–2284. https://doi.org/10.1016/j.jeurceramsoc.2011.05.042.

(27) Du, M.; Bi, J.-Q.; Wang, W.-L.; Sun, X.-L.; Long, N.-N. Microstructure and Properties of SiO2 Matrix Reinforced by BN Nanotubes and Nanoparticles. *Journal of Alloys and Compounds* **2011**, *509* (41), 9996–10002. https://doi.org/10.1016/j.jallcom.2011.08.010.

(28) Tank, M.; Leon, A. D.; Huang, W.; Patadia, M.; Degraff, J.; Sweat, R. Manufacturing of Stereolithographic 3D Printed Boron Nitride Nanotube-Reinforced Ceramic Composites with Improved Thermal and Mechanical Performance. *Funct. Compos. Struct.* **2023**, *5* (1), 015001. https://doi.org/10.1088/2631-6331/acb12a.

(29) Du, M.; Bi, J.-Q.; Wang, W.-L.; Sun, X.-L.; Long, N.-N. Influence of Sintering Temperature on Microstructure and Properties of SiO2 Ceramic Incorporated with Boron Nitride Nanotubes. *Materials Science and Engineering: A* **2012**, *543*, 271–276. https://doi.org/10.1016/j.msea.2012.02.065.

(30) Du, M.; Bi, J.-Q.; Wang, W.-L.; Sun, X.-L.; Long, N.-N.; Bai, Y.-J. Fabrication and Mechanical Properties of SiO2–Al2O3–BNNPs and SiO2–Al2O3–BNNTs Composites. *Materials Science and Engineering: A* **2011**, *530*, 669–674. https://doi.org/10.1016/j.msea.2011.10.008.

(31) Tatarko, P.; Grasso, S.; Chlup, Z.; Porwal, H.; Kašiarová, M.; Dlouhý, I.; Reece, M. J. Toughening Effect of Multi-Walled Boron Nitride Nanotubes and Their Influence on the Sintering Behaviour of 3Y-TZP Zirconia Ceramics. *Journal of the European Ceramic Society* **2014**, *34* (7), 1829–1843. https://doi.org/10.1016/j.jeurceramsoc.2013.12.046.

(32) Wang, S.; Wang, G.; Wen, D.; Yang, X.; Yang, L.; Guo, P. Mechanical Properties and Thermal Shock Resistance Analysis of BNNT/Si3N4 Composites. *Appl Compos Mater* **2018**, *25* (2), 415–423. https://doi.org/10.1007/s10443-017-9627-3.

(33) Li, T.; Chen, Y.; Li, W.; Li, J.; Luo, L.; Yang, T.; Liu, L.; Wu, G. Fabrication and Mechanical Properties of Boron Nitride Nanotube Reinforced Silicon Nitride Ceramics. *Ceramics International* **2018**, *44* (6), 6456–6460. https://doi.org/10.1016/j.ceramint.2018.01.041.

(34) Wang, W.-L.; Bi, J.-Q.; Sun, K.-N.; Du, M.; Long, N.-N.; Bai, Y.-J. Fabrication of Alumina Ceramic Reinforced with Boron Nitride Nanotubes with Improved Mechanical Properties. *J. Am. Ceram. Soc.* **2011**, *94* (11), 3636–3640. https://doi.org/10.1111/j.1551-2916.2011.04821.x.

(35) Zhu, G.; Dong, S.; Ni, D.; Xu, C.; Wang, D. Microstructure, Mechanical Properties and Oxidation Resistance of SiCf/SiC Composites Incorporated with Boron Nitride Nanotubes. *RSC Adv.* **2016**, *6* (86), 83482–83492. https://doi.org/10.1039/C6RA16496J.

(36) Du, M.; Bi, J.-Q.; Wang, W.-L.; Sun, X.-L.; Long, N.-N. Microstructure and Properties of SiO2 Matrix Reinforced by BN Nanotubes and Nanoparticles. *Journal of Alloys and Compounds* **2011**, *509* (41), 9996–10002. https://doi.org/10.1016/j.jallcom.2011.08.010.

(37) Tang, C.; Fang, Z.; Wang, D.; Jin, X.; Ran, S. Comparison of TiB2–h-BN Composites Prepared by Reactive and Conventional Spark Plasma Sintering. *Ceramics International* **2023**, *49* (14, Part A), 23091–23098. https://doi.org/10.1016/j.ceramint.2023.04.137.

(38) Liang, H.; Liu, J.; Zou, J.; Huang, J.; Wang, W.; Fu, Z. Processing and Properties of Reactively Densified TiB2-AlN-hBN Conductive Ceramics with Tunable Compositions. *Journal of the European Ceramic Society* **2023**, *43* (8), 3013–3024. https://doi.org/10.1016/j.jeurceramsoc.2023.01.053.

(39) Smith, M. W.; Jordan, K. C.; Park, C.; Kim, J.-W.; Lillehei, P. T.; Crooks, R.; Harrison, J. S. Very Long Single- and Few-Walled Boron Nitride Nanotubes via the Pressurized Vapor/Condenser Method. *Nanotechnology* **2009**, *20* (50), 505604. https://doi.org/10.1088/0957-4484/20/50/505604.

(40) Zheng, M.; Ke, C.; Bae, I.-T.; Park, C.; Smith, M. W.; Jordan, K. Radial Elasticity of Multi-Walled Boron Nitride Nanotubes. *Nanotechnology* **2012**, *23* (9), 095703. https://doi.org/10.1088/0957-4484/23/9/095703.

(41) Yamakov, V.; Park, C.; Kang, J. H.; Chen, X.; Ke, C.; Fay, C. Piezoelectric and Elastic Properties of Multiwall Boron-Nitride Nanotubes and Their Fibers: A Molecular Dynamics Study. *Computational Materials Science* **2017**, *135*, 29–42. https://doi.org/10.1016/j.commatsci.2017.03.050.

(42) Kundalwal, S. I.; Rathi, A. Improved Mechanical and Viscoelastic Properties of CNT-Composites Fabricated Using an Innovative Ultrasonic Dual Mixing Technique. *Journal of the Mechanical Behavior of Materials* **2020**, *29* (1), 77–85. https://doi.org/10.1515/jmbm-2020-0008.

(43) Neuber, H. *Theory of Notch Stresses: Principles for Exact Calculation of Strength with Reference to Structural Form and Material*, Second enlarged edition.; Translation series (U.S. Atomic Energy Commission); USAEC Office of Technical Information: Oak Ridge, Tenn., 1961.

(44) Novozhilov, V. V. On a Necessary and Sufficient Criterion for Brittle Strength: PMM Vol. 33, N≝2, 1969, Pp. 212–222. *Journal of Applied Mathematics and Mechanics* **1969**, *33* (2), 201–210. https://doi.org/10.1016/0021-8928(69)90025-2.

(45) Leguillon, D.; Martin, É.; Lafarie-Frenot, M.-C. Flexural vs. Tensile Strength in Brittle Materials. *Comptes Rendus Mécanique* **2015**, *343* (4), 275–281. https://doi.org/10.1016/j.crme.2015.02.003.

(46) Klein, C. Characteristic Strength, Weibull Modulus, and Failure Probability of Fused Silica Glass. *Optical Engineering - OPT ENG* **2009**, *48*. https://doi.org/10.1117/1.3265716.

(47) *Roark's Formulas for Stress and Strain*, 9th Edition.; McGraw-Hill Education, 2020.

(48) Anjum, N.; Alsmairat, O. Q.; Liu, Z.; Park, C.; Fay, C. C.; Ke, C. Mechanical Characterization of Electrospun Boron Nitride Nanotube-Reinforced Polymer Nanocomposite Microfibers. *Journal of Materials Research* **2022**. https://doi.org/10.1557/s43578-022-00653-8.

(49) Alsmairat, O. Q.; Gou, F.; Dmuchowski, C. M.; Chiarot, P. R.; Park, C.; Miles, R. N.; Ke, C. Quantifying the Interfacial Load Transfer in Electrospun Carbon Nanotube Polymer Nanocomposite Microfibers by Using in Situ Raman Micromechanical Characterization Techniques. *J. Phys. D: Appl. Phys.* **2020**, *53* (36), 365302. https://doi.org/10.1088/1361-6463/ab8fdd.

(50) Zhang, S. C.; Hilmas, G. E.; Fahrenholtz, W. G. Pressureless Sintering of ZrB2–SiC Ceramics. *Journal of the American Ceramic Society* **2008**, *91* (1), 26–32. https://doi.org/10.1111/j.1551-2916.2007.02006.x.

(51) Arenal, R.; Ferrari, A. C.; Reich, S.; Wirtz, L.; Mevellec, J. Y.; Lefrant, S.; Rubio, A.; Loiseau, A. Raman Spectroscopy of Single-Wall Boron Nitride Nanotubes. *Nano Letters* **2006**, *6* (8), 1812–1816. https://doi.org/10.1021/nl0602544.

(52) Nemanich, R. J.; Solin, S. A.; Martin, R. M. Light Scattering Study of Boron Nitride Microcrystals. *Physical Review B* **1981**, *23* (12), 6348–6356. https://doi.org/10.1103/PhysRevB.23.6348.

(53) Wang, W.; Li, Z.; Prestat, E.; Hashimoto, T.; Guan, J.; Kim, K. S.; Kingston, C. T.; Simard, B.; Young, R. J. Reinforcement of Polymer-Based Nanocomposites by Thermally Conductive and Electrically Insulating Boron Nitride Nanotubes. *ACS Appl. Nano Mater.* **2020**, *3* (1), 364–374. https://doi.org/10.1021/acsanm.9b02010.

(54) Fakrach, B.; Rahmani, A.; Chadli, H.; Sbai, K.; Sauvajol, J.-L. Raman Spectrum of Single-Walled Boron Nitride Nanotube. *Physica E: Low-dimensional Systems and Nanostructures* **2009**, *41* (10), 1800–1805. https://doi.org/10.1016/j.physe.2009.07.002.

(55) Carlotti, G.; Doucet, L.; Dupeux, M. Elastic Properties of Silicon Dioxide Films Deposited by Chemical Vapour Deposition from Tetraethylorthosilicate. *Thin Solid Films* **1997**, *296* (1), 102–105. https://doi.org/10.1016/S0040-6090(96)09346-7.

(56) Zeng, J.; Saltysiak, B.; Johnson, W. S.; Schiraldi, D. A.; Kumar, S. Processing and Properties of Poly(Methyl Methacrylate)/Carbon Nano Fiber Composites. *Composites Part B: Engineering* **2004**, *35* (2), 173–178. https://doi.org/10.1016/S1359-8368(03)00051-9.

(57) Yu, J.; Wang, H.; Zhang, J.; Zhang, D.; Yan, Y. Gelcasting Preparation of Porous Silicon Nitride Ceramics by Adjusting the Content of Monomers. *J Sol-Gel Sci Technol* **2010**, *53* (3), 515–523. https://doi.org/10.1007/s10971-009-2125-9.

(58) Ning, J.; Zhang, J.; Pan, Y.; Guo, J. Fabrication and Mechanical Properties of SiO2 Matrix Composites Reinforced by Carbon Nanotube. *Materials Science and Engineering: A* **2003**, *357* (1), 392–396. https://doi.org/10.1016/S0921-5093(03)00256-9.

(59) Suplicz, A.; Szabo, F.; Kovacs, J. G. Injection Molding of Ceramic Filled Polypropylene: The Effect of Thermal Conductivity and Cooling Rate on Crystallinity. *Thermochimica Acta* **2013**, *574*, 145–150. https://doi.org/10.1016/j.tca.2013.10.005.

(60) Denry, I.; Holloway, J. A. Ceramics for Dental Applications: A Review. *Materials* **2010**, *3* (1), 351–368. https://doi.org/10.3390/ma3010351.

(61) Kazemi, A.; Faghihi-Sani, M. A.; Alizadeh, H. R. Investigation on Cristobalite Crystallization in Silica-Based Ceramic Cores for Investment Casting. *Journal of the European Ceramic Society* **2013**, *33* (15), 3397–3402. https://doi.org/10.1016/j.jeurceramsoc.2013.06.025.

(62) Nazari, F.; Honarpisheh, M.; Zhao, H. The Effect of Microstructure Parameters on the Residual Stresses in the Ultrafine-Grained Sheets. *Micron* **2020**, *132*, 102843. https://doi.org/10.1016/j.micron.2020.102843.

(63) Li, Z.; Xiong, M.; Lei, J.; Li, J.; Chen, Y.; Zhang, S. Effect of Mo Doping on the Microstructures and Mechanical Properties of ZnO and AZO Ceramics. *Ceramics International* **2021**, *47* (21), 30563–30571. https://doi.org/10.1016/j.ceramint.2021.07.234.

## Table of Content Graphics